


# Fast and accurate reconstruction of human lung gas MRI with deep learning

Caohui Duan<sup>1,2</sup> | He Deng<sup>1,2</sup> | Sa Xiao<sup>1,2</sup> | Junshuai Xie<sup>1,2</sup> | Haidong Li<sup>1,2</sup> |  
Xianping Sun<sup>1,2</sup> | Lin Ma<sup>3</sup> | Xin Lou<sup>3</sup> | Chaohui Ye<sup>1,2</sup> | Xin Zhou<sup>1,2</sup> 

<sup>1</sup>State Key Laboratory of Magnetic Resonance and Atomic and Molecular Physics, National Center for Magnetic Resonance in Wuhan, Wuhan Institute of Physics and Mathematics, Chinese Academy of Sciences - Wuhan National Laboratory for Optoelectronics, Wuhan, P. R. China

<sup>2</sup>University of Chinese Academy of Sciences, Beijing, P. R. China

<sup>3</sup>Department of Radiology, Chinese PLA General Hospital, Beijing, P. R. China

## Correspondence

Xin Zhou, Wuhan Institute of Physics and Mathematics, Chinese Academy of Sciences, 30 West Xiaohongshan, Wuhan, 430071, P. R. China.  
Email: xinzhou@wipm.ac.cn

## Funding information

This work is supported by National Natural Science Foundation of China (81625011, 81771917, 91859206, 81730048, 81825012), National Key R&D Program of China (2016YFC1304700), Key Research Program of Frontier Sciences, CAS (QYZDY-SSW-SLH018) and Hubei Provincial Natural Science Foundation of China (2017CFA013, 2018ACA143).

**Purpose:** To fast and accurately reconstruct human lung gas MRI from highly undersampled k-space using deep learning.

**Methods:** The scheme was comprised of coarse-to-fine nets (C-net and F-net). Zero-filling images from retrospectively undersampled k-space at an acceleration factor of 4 were used as input for C-net, and then output intermediate results which were fed into F-net. During training, a L2 loss function was adopted in C-net, while a function that united L2 loss with proton prior knowledge was used in F-net. The 871 hyperpolarized <sup>129</sup>Xe pulmonary ventilation images from 72 volunteers were randomly arranged as training (90%) and testing (10%) data. Ventilation defect percentage comparisons were implemented using a paired 2-tailed Student's *t*-test and correlation analysis. Furthermore, prospective acquisitions were demonstrated in 5 healthy subjects and 5 asymptomatic smokers.

**Results:** Each image with size of 96 × 84 could be reconstructed within 31 ms (mean absolute error was 4.35% and structural similarity was 0.7558). Compared with conventional compressed sensing MRI, the mean absolute error decreased by 17.92%, but the structural similarity increased by 6.33%. For ventilation defect percentage, there were no significant differences between the fully sampled and reconstructed images through the proposed algorithm ( $P = 0.932$ ), but had significant correlations ( $r = 0.975$ ;  $P < 0.001$ ). The prospectively undersampled results validated a good agreement with fully sampled images, with no significant differences in ventilation defect percentage but significantly higher signal-to-noise ratio values.

**Conclusion:** The proposed algorithm outperformed classical undersampling methods, paving the way for future use of deep learning in real-time and accurate reconstruction of gas MRI.

## KEYWORDS

convolutional neural networks, deep learning, hyperpolarized gas, image reconstruction, MRI

## 1 | INTRODUCTION

MRI is a non-invasive and radiation-free technique, providing high-resolution images of anatomical structures and physiological functions. However, conventional  $^1\text{H}$  MRI is challenging to use for the lung because of the low proton spin density throughout the lung tissue. Hyperpolarized (HP) gas MRI (e.g.,  $^3\text{He}$  or  $^{129}\text{Xe}$ ) has been used for human lung structure and function imaging.<sup>1</sup> In particular, HP  $^{129}\text{Xe}$  MRI is able to evaluate gas exchange and uptake due to the good solubility of xenon in blood and tissues.<sup>1,2</sup> Nevertheless, the longitudinal magnetization of HP gas is nonrenewable, which imposes limits on MRI acquisition.<sup>3</sup> Moreover, most HP gas MRI methods acquire data during a single breath-hold, but long breath-holding time imposes burdens on subjects, especially for those patients with compromised respiratory function. Accordingly, various efforts have focused on accelerating the acquisition of HP gas MRI, including methods based on parallel imaging,<sup>4</sup> radial,<sup>5</sup> spiral,<sup>6</sup> compressed sensing MRI (CS-MRI),<sup>7</sup> or the combination of these techniques.<sup>8,9</sup> Among them, CS-MRI is a good solution to shorten scan time by undersampling measurements in k-space, and without additional hardware required.<sup>10</sup>

Ajraoui et al first applied CS to reconstruct HP  $^3\text{He}$  lung images at an acceleration factor (AF) of 2 for 2D images and 5 for 3D ventilation images.<sup>11</sup> Combining some prior knowledge, an AF of 3 was achieved for 2D images with less reconstruction errors.<sup>12</sup> Moreover, CS was used to facilitate multiple  $b$ -value  $^3\text{He}/^{129}\text{Xe}$  diffusion-weighted MRI during a single breath-hold.<sup>13,14</sup> However, conventional CS-MRI had some limitations: (1) The sparse transforms (e.g., total variation<sup>15</sup> or discrete wavelet transform<sup>10</sup>) could be inadequate to describe complex image contents, especially for biological tissues. This could lead to artifacts and loss of detailed structures in reconstructed results.<sup>16,17</sup> (2) CS used iterative strategies to optimize some objective functions, which was typically time-consuming. (3) The choice of hyper-parameters (e.g., update rates, weighting parameters) was tedious, which possibly caused excessively smooth or residual undersampling artifacts in reconstructed results.<sup>16</sup> Therefore, effective reconstruction methods are needed to be explored.

Recently, deep learning has been successfully applied in many computer vision problems.<sup>18</sup> In particular, convolutional neural networks (CNNs) are becoming the state-of-the-art strategies for image classification,<sup>19</sup> super-resolution,<sup>20</sup> restoration,<sup>21</sup> and segmentation.<sup>22</sup> Meanwhile, CNNs based MRI reconstruction, such as variational network<sup>16</sup> and deep de-aliasing generative adversarial networks,<sup>17</sup> has also been validated significant improvements over CS-MRI regarding reconstruction quality and speed.<sup>23</sup> Such methods learn the nonlinear mapping between the undersampled images or k-space and reference images by training CNNs.<sup>24,25</sup> Currently, most of the CNNs methods

take fully sampled (FS) images as references and focus on brain or knee MRI, which have large amounts of high-resolution and signal-to-noise ratio (SNR) training data.<sup>24-26</sup> However, HP gas MRI is susceptible to noise or artifacts due to the nonrenewability of HP magnetization.<sup>3</sup> Thus, it is expensive or difficult to obtain multiple high-quality HP gas images. Moreover, as the noise level increases, the reconstruction results using CNNs become more blurred.<sup>16,25</sup> Therefore, it may not be effective to directly apply CNNs into the reconstruction of HP gas MRI.

It is known that some prior knowledge (e.g., organ structure) has potential to improve the performance of image analysis, especially for cases where images are corrupted or contain artifacts due to limitations in image acquisition.<sup>27</sup> For example, the performance of CS-MRI was improved by incorporating the prior knowledge of polarization decay and mutual anatomical information from proton ( $^1\text{H}$ ) images.<sup>12</sup> By uniting anatomical prior knowledge into CNNs, a generic training strategy achieved the state-of-the-art prediction accuracy in image segmentation.<sup>27</sup> Similarly, if some prior knowledge (such as lung structure and/or boundaries) is integrated into a CNNs model, the reconstruction performance of HP gas MRI will be improved.

In this work, we first propose a cascaded CNNs model incorporating prior knowledge of  $^1\text{H}$  images (called as CasNet) to reconstruct HP gas images from highly undersampled k-space. We expect that the CasNet is able to reconstruct the real-time human lung, while not only removing aliasing artifacts but also refining structural details of the lung.

## 2 | METHODS

### 2.1 | Cascaded CNNs

Assume that  $\mathbf{x} \in \mathbf{C}^N$  denotes a desired HP gas MR image, which needs to be reconstructed from the undersampled k-space  $\mathbf{y} \in \mathbf{C}^M$  ( $M \ll N$ ), that is,

$$\mathbf{y} = \mathbf{F}_u \mathbf{x} + \mathbf{n} \quad (1)$$

where  $\mathbf{F}_u \in \mathbf{C}^{M \times N}$  denotes an undersampled Fourier encoding matrix and  $\mathbf{n} \in \mathbf{C}^M$  denotes the acquisition noise. Under conditions of Cartesian undersampling patterns,  $\mathbf{F}_u = \mathbf{U}\mathbf{F}$ , where  $\mathbf{U}$  is an undersampled mask and  $\mathbf{F}$  is 2D Fourier transform. However, the reconstruction of  $\mathbf{x}$  from  $\mathbf{y}$  is an ill-posed problem owing to  $M \ll N$ . CS-MRI usually solves such issue through an unconstrained optimization strategy.<sup>10</sup>

Different to CS-MRI, the CasNet reconstructs  $\mathbf{x}$  by training CNNs models (see Figure 1), which includes 1 coarse net (named as C-net) and 1 fine net (named as F-net). The

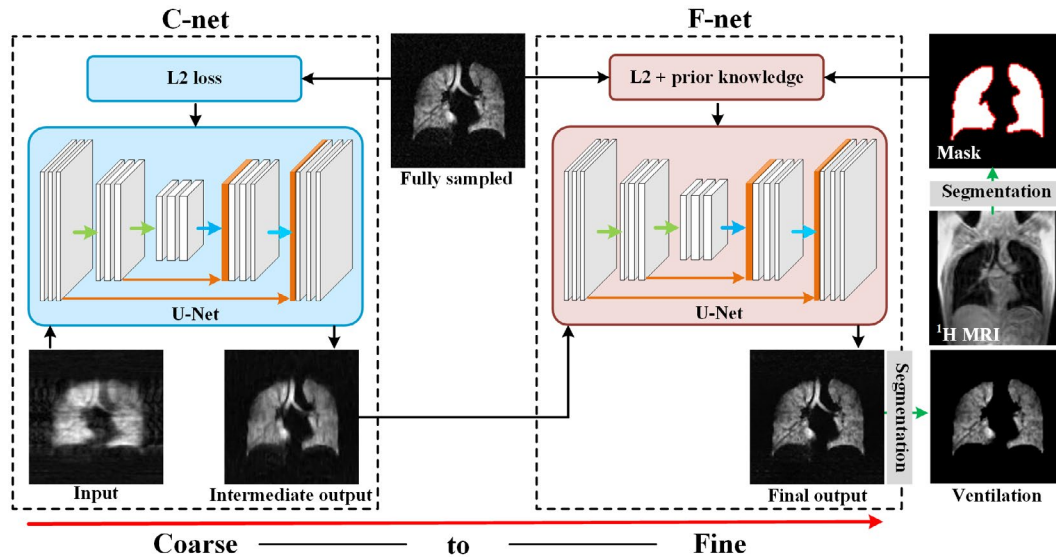


**FIGURE 1** The scheme of the CasNet for undersampled reconstruction of human lung gas MRI. The C-net takes zero-filling images as inputs and then outputs coarse reconstruction results. The intermediate results are fed into the F-net for further improving structural details of the lung

C-net aims to eliminate image aliasing and find the following minimization.

$$\operatorname{argmin}_{\mathbf{x}_C} \|\mathbf{x} - \mathbf{x}_C\|_2^2 = \operatorname{argmin}_{\theta_C} \|\mathbf{x} - C(\mathbf{x}_0; \theta_C)\|_2^2 \quad (2)$$

where  $\mathbf{x}_C$  is the coarse estimation of  $\mathbf{x}$ , and  $\mathbf{x}_0$  is the zero-filling result. The C-net,  $C$ , takes  $\mathbf{x}_0$  as input and adopts unknown parameters  $\theta_C$ . We use FS images as references during training. Because the references are typically corrupted with noise due to the nonrenewable HP magnetization, the intermediate results  $\mathbf{x}_C$  may become blurred<sup>16,25</sup> and lose structural details of the lung (see Figure 1). Consequently, C-net is cascaded into F-net, aiming to refine structural details within the lung region. The F-net is to solve the following minimization.

$$\operatorname{argmin}_{\mathbf{x}_F} \|\mathbf{x} - \mathbf{x}_F\|_2^2 = \operatorname{argmin}_{\theta_F} \|\mathbf{x} - F(\mathbf{x}_C; \theta_F)\|_2^2 \quad (3)$$

where  $\mathbf{x}_F$  is the fine estimation of  $\mathbf{x}$ ,  $\cdot$  is the element-wise multiplication, and  $\mathbf{m}$  is the prior knowledge. The F-net,  $F$ , takes  $\mathbf{x}_C$  as input and uses unknown parameters  $\theta_F$ . In this work, lung boundaries obtained from  $^1\text{H}$  images are taken as prior knowledge because there is no HP gas signal outside the lung mask (see Figure 1). Then  $\mathbf{m}$  is described as,

$$\mathbf{m}_i = \begin{cases} 1 & \text{if } i \in \Omega \\ 0 & \text{else,} \end{cases} \quad (4)$$

where  $i$  is the pixel index, and  $\Omega$  is the lung region.  $\mathbf{m}$  is a binary mask, which indicates the lung and background noise. In

this way, the reconstruction is constrained in the lung region, which potentially improves structural details of the lung. Note that  $^1\text{H}$  and HP gas images are acquired in the same breath-hold, and then these images are well spatially registered.<sup>28</sup> Combining Equations 2 and 3, the target objective function can be defined as,

$$\operatorname{argmin}_{\theta_C, \theta_F} \left\| (\mathbf{x} - F(C(\mathbf{x}_0; \theta_C); \theta_F)) \cdot \mathbf{m} \right\|_2^2. \quad (5)$$

## 2.2 | Network architecture

U-Net based architecture is used in both the C-net and F-net because it has some advantages, such as multilevel decomposition, multichannel filtering and multiscale skip connections.<sup>22,29</sup> U-Net has been successfully applied for MRI or CT reconstruction.<sup>29,30</sup> The detailed architecture of U-Net is displayed in Figure 2, which comprises a contracting path and an expansive path. In the contracting path, each stage contains 2 sequential  $3 \times 3$  convolution layers with stride 1, and each convolution layer is followed by batch normalization<sup>31</sup> and rectified linear unit activation. Then a  $2 \times 2$  max pooling with stride 2 is applied. Thus, the size of feature maps is halved after each pooling layer. If the size of input image is  $96 \times 96$ , the size of feature maps will become  $6 \times 6$  in the last stage. Note that zero-padding is adopted for each convolution layer so that the size of feature maps does not decrease after convolution. In the expansive path, each stage starts with a  $3 \times 3$  up-convolution layer with stride 2, followed by batch normalization and rectified linear unit activation. The up-convolution layer doubles the size of feature maps and

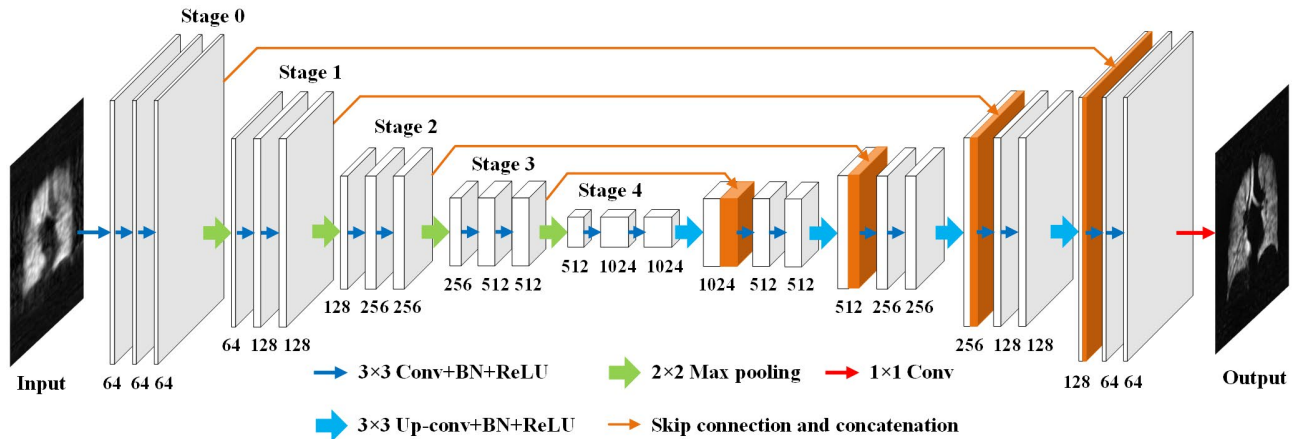


**FIGURE 2** The detailed architecture of U-Net. The number of channels is denoted below each feature map. Note that Conv denotes convolution; Up-conv denotes up-convolution

halves the number of channels. Then the up-convolution output is concatenated with the mirrored feature maps from the contracting path. The final layer only contains a  $1 \times 1$  convolution layer to combine 64 feature maps into the output image.

### 2.3 | Data acquisition and preprocessing

Seventy-two subjects were enrolled for this study after providing informed consents, including 30 healthy, 2 asthma, 9 chronic obstructive pulmonary disease (COPD), 2 bronchiectasis (BE), 9 chronic inflammation (CI), 2 pulmonary tuberculosis (PT), and 16 pulmonary nodule (PN) subjects (see Table 1 for the details about subjects' information). All experiments were approved by the local Institutional Review Board. Experiments were performed on a 1.5T whole-body MRI scanner (Avanto, Siemens Medical Solutions). Enriched  $^{129}\text{Xe}$  gas [1% enriched xenon (86%  $^{129}$ -isotope), 89%  $^4\text{He}$ , and 10%  $\text{N}_2$ ] was polarized by means of spin-exchange optical pumping with "freeze-out" accumulating in a cold finger using a home-built xenon polarizer. Then, 500 mL HP  $^{129}\text{Xe}$

was thawed into a Tedlar bag and mixed with 500 mL medical grade  $\text{N}_2$ . The available polarization was approximately 25% in the bag. After that, the subjects were instructed to inhale the gas mixture from functional residual capacity, and then hold their breath for data acquisition.

The MRI parameters for HP  $^{129}\text{Xe}$  imaging<sup>32</sup> were: repetition time/echo time (TR/TE) = 4.2/1.9 ms, matrix size =  $96 \times 84$ , field of view =  $384 \times 336 \text{ mm}^2$ , slice thickness = 8 mm, bandwidth = 38.4 kHz, number of slices = 24, 3D bSSFP sequence, flip angle (FA) =  $10^\circ$ , scan time = 8.4 s. During the same breath-hold, anatomic  $^1\text{H}$  images were acquired after  $^{129}\text{Xe}$  MR imaging. The MRI parameters for  $^1\text{H}$  imaging were: TR/TE = 2.4/0.7 ms, matrix size =  $96 \times 84$ , field of view =  $384 \times 336 \text{ mm}^2$ , slice thickness = 8 mm, bandwidth = 48 kHz, number of slices = 24, 3D FLASH sequence, FA =  $5^\circ$ , scan time = 2 s. The total acquisition time, including the time delay between the 2 scans, was approximately 11 s.

Due to lack of HP gas signal or high-level noise, we removed those slices whose SNR was less than 6.6 because such slices could not meet the requirements of image analysis.<sup>33</sup> After that, 871 HP  $^{129}\text{Xe}$  ventilation images and same-breath

**TABLE 1** Subjects' information grouped by broad classes of clinical indications

Clinical indications	Age (mean $\pm$ SD)	Subject number		Image number	
		Male	Female	Train	Test
Healthy	36.7 $\pm$ 12.3	17	13	353	33
Asthma	43.5 $\pm$ 23.3	0	2	23	2
COPD	58.0 $\pm$ 12.9	8	1	78	10
BE	60.5 $\pm$ 24.7	2	0	22	6
CI	59.6 $\pm$ 11.3	9	2	113	6
PT	66.5 $\pm$ 21.9	1	1	20	7
PN	52.7 $\pm$ 11.7	7	9	174	23
Total	48.1 $\pm$ 16.0	44	28	784	87

Abbreviations: COPD, chronic obstructive pulmonary disease; BE, bronchiectasis; CI, chronic inflammation; PT, pulmonary tuberculosis; PN, pulmonary nodule; SD, standard deviation.

anatomic  $^1\text{H}$  images were obtained from 72 subjects. Table 1 listed the subjects' information grouped by broad classes of clinical indications. A total of 784 images (90%) were randomly chosen for training the CasNet, and the other 87 images (10%) for testing its performance. To reduce overfitting and improve the performance of CasNet, we applied data augmentation on the training set.<sup>23</sup> Particularly, we rotated the original images by  $90^\circ$ ,  $180^\circ$ ,  $270^\circ$ , and flipped original ones horizontally. This generated 4 additional augmented images for each original image. Thus, the total number of training images was 3920.

During training and testing, FS images were considered as references. Zero-filling images were taken as inputs in the C-net, which were obtained by retrospectively undersampling the reference k-space data in 1 phase-encoding direction ( $k_y$ ) according to a variable-density Cartesian random undersampling matrix. The matrix was generated using a Monte Carlo algorithm at an AF of 4.<sup>10</sup> Because both the input and output were the real-valued data type, all training and testing data were transformed into magnitude images. Furthermore, each image was normalized to  $[0, 1]$ , then the normalized images were padded to  $96 \times 96$ , aiming to be compatible with U-Net architecture.

To validate the performance of CasNet for in vivo imaging, the FS and undersampled data (the AF was set to 4) were prospectively acquired from 5 healthy subjects (age,  $25.6 \pm 2.4$  years) and 5 asymptomatic smokers (age,  $54.2 \pm 11.3$  years) with a smoking history of at least 12 pack-years. For the FS acquisition, the FA was set to  $10^\circ$ . According to the effects of k-space filter<sup>34</sup> and signal evolutions in k-space center,<sup>11,35,36</sup> the FA was set to  $15^\circ$  for the undersampled acquisition. The undersampled acquisition adopted a custom pulse sequence, which could faithfully reproduce the undersampling pattern used in the retrospective analysis.

## 2.4 | Implementation and training

The CasNet was implemented through the MatConvNet toolbox (ver.24)<sup>37</sup> in the MATLAB 2017a environment (MathWorks, Natick, MA). Training and testing were performed on a desktop computer with an NVIDIA TITAN Xp GPU and an Intel Xeon(R) E5-2407 CPU.

Because of a large number of parameters and deep layers in the CasNet, we used incremental manner to train the C-net and F-net separately, aiming to avoid overfitting and memory shortages.<sup>25</sup> The hyper-parameters were: momentum = 0.9, weight decay =  $10^{-4}$ , and batch size = 16. The learning rate was logarithmically reduced at each epoch from  $10^{-2}$  to  $10^{-5}$  during the first 30 epochs. The gradient clipping parameter for the C-net was  $10^{-3}$ , and  $10^{-5}$  for the F-net. Then, the Xavier method was used to initialize all the network parameters,<sup>38</sup> and these parameters were optimized through the stochastic gradient descent with momentum

approach. The training was stopped after 100 epochs. It took approximately 4 h to train each network and total 8 h for the CasNet.

## 2.5 | Performance evaluation

To evaluate the efficacy of fine stage in the CasNet, the reconstruction results through the C-net and F-net were compared in a cascaded manner. Because CS-MRI could achieve the state-of-the-art reconstruction from under-sampled HP gas data, the CasNet was compared with CS-MRI,<sup>11,39</sup> which was to solve the following minimization equation.

$$\underset{\mathbf{x}}{\operatorname{argmin}} \|\mathbf{F}_u \mathbf{x} - \mathbf{y}\|_2^2 + \lambda_1 \|\Psi \mathbf{x}\|_1 + \lambda_2 TV(\mathbf{x}) \quad (6)$$

where  $\Psi$  was the sparsifying transform (here lifting-scheme wavelet<sup>40,41</sup>),  $TV$  was the total variation regularization, and  $\lambda_1, \lambda_2$  were weighting parameters to balance data fidelity and artifact reduction. The CS-MRI was also implemented in MATLAB. The weighting parameters were estimated individually for each reconstruction by means of the grid search strategy that minimized the mean absolute error (MAE) between the reconstructed and FS images.<sup>16</sup>

Because the MAE and structural similarity (SSIM)<sup>42</sup> were widely used to evaluate the reconstruction performance, we adopted such indexes to quantitatively assess the performance through the C-net, F-net, and CS-MRI. The MAE was used to evaluate the mean absolute difference between the reference and reconstructed images,<sup>11</sup> while the SSIM was to evaluate the structure similarity between those images. Both the MAE and SSIM were computed over the lung region defined by a mask segmented from  $^1\text{H}$  images. From the definition, lower MAE or higher SSIM values indicated better reconstruction quality.

Moreover, HP gas ventilation images could estimate ventilation defects for patients with obstructive lung diseases, such as COPD and asthma.<sup>43</sup> When combined with spatially registered  $^1\text{H}$  images of the lung, ventilation defect percentage (VDP) was a commonly used quantitative metric of lung function. VDP was defined by the ratio of the ventilation defect volume in HP gas images to the thoracic cavity volume in  $^1\text{H}$  images, which required the definition of ventilation defect regions in HP gas images through the hierarchical k-means cluster<sup>44</sup> and the thoracic cavity mask by means of the region growing in  $^1\text{H}$  ones.

A Bland-Altman plot was to assess the consistency of VDP between the reference and reconstructed images through the CasNet. Moreover, a paired 2-tailed Student's  $t$ -test was used to test whether there were significant differences regarding VDP between the reconstructed and reference images, and Pearson correlation coefficients ( $r$  values) were used to evaluate their relationship.  $P < 0.05$  was considered statistically significant.

### 3 | RESULTS

#### 3.1 | C-net versus F-net

Figure 3 depicts the FS and reconstructed images obtained using the zero-filling, C-net and F-net of the 16<sup>th</sup> slice of the lung from a healthy volunteer (A1-D1), and the 10<sup>th</sup> slice from a PT subject (A2-D2). It can be seen that there exist severe oscillatory artifacts, and most of the lung structures are lost in Figure 3B1,B2. After the C-net, the undersampling artifacts are successfully removed and the detailed structures are restored to some extent (see Figure 3C1,C2). However, some details are blurred owing to the high AF, especially in green boxes. Through the F-net, those blurred details are restored and sharpened, especially in lung edges and low ventilation regions (see Figure 3D1,D2). Meanwhile, the MAE and SSIM metrics are listed under the images. It can be found that the F-net owns the lowest MAE and highest SSIM values.

Table 2 lists the average MAE and SSIM values obtained using different algorithms for the healthy, asthma, COPD, BE, CI, PT, and PN test data, respectively. The total average MAE and SSIM values are listed in the last row of Table 2. Compared with zero-filling images, C-net and F-net own

lower MAE and higher SSIM values. In comparison with C-net, F-net leads to the decrease of MAE by 4.09%, 3.73%, 5.73%, 12.50%, 5.71%, 8.96%, and 4.29% for the 7 test sets, while the increase of SSIM by 3.29%, 3.77%, 2.45%, 6.30%, 4.09%, 3.57%, and 3.12%, respectively.

#### 3.2 | CS-MRI versus CasNet

Figure 4 shows the FS images and reconstructed results through the zero-filling, CS-MRI, and CasNet. For a COPD subject, Figure 4A1 shows the FS image of the 14<sup>th</sup> slice of the lung, and the retrospectively undersampled results are displayed in Figure 4B1,C1,D1. We can see that there are large focal ventilation defects within the lung in Figure 4A1. However, the artifacts in Figure 4B1 cover the ventilation defects. After the CS-MRI, the artifacts are slightly removed and the fine details are restored to some extent, but unnatural block patterns are produced, as shown in Figure 4C1. Through the CasNet, the aliasing artifacts are successfully removed and most of the details are restored, as displayed in Figure 4D1.

Figure 4A2 shows the FS image of the 11<sup>th</sup> slice of the lung from a PN subject, and the reconstructed results

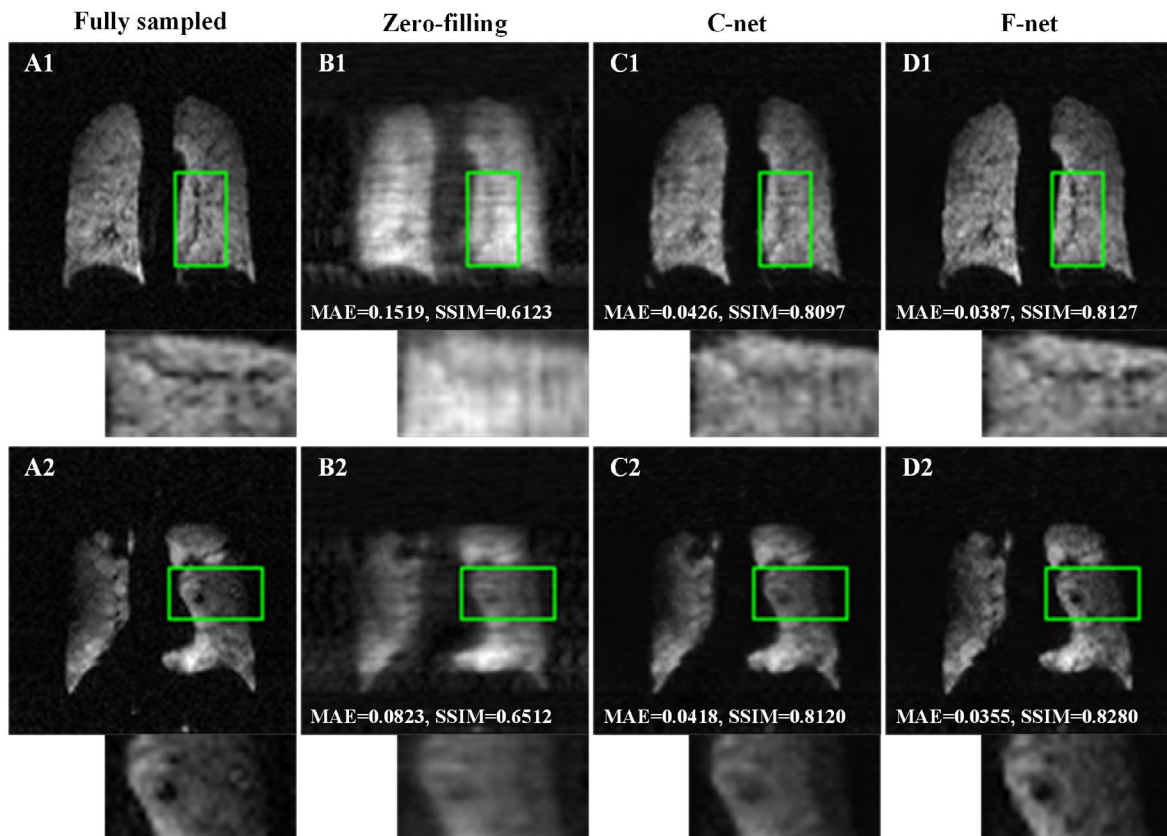


**FIGURE 3** Reconstructed results obtained using the zero-filling, C-net, and F-net at an AF of 4. A1, One slice of FS image from a healthy volunteer. A2, One slice of FS image from a PT subject. B1-B2,C1-C2,D1-D2, Reconstructed results through the zero-filling, C-net, and F-net, respectively. Magnified regions of green boxes are placed at the right bottom of the corresponding images. The quantitative metrics are also listed under the images

**TABLE 2** Average MAE and SSIM values obtained using the zero-filling, CS-MRI, C-net, and F-net for the 7 test sets at an AF of 4

Clinical indications	Zero-filling MAE/SSIM	CS-MRI MAE/SSIM	C-net MAE/SSIM	F-net MAE/SSIM <sup>a</sup>
Healthy	0.1113/0.6016	0.0537/0.7166	0.0440/0.7409	<b>0.0422/0.7653</b>
Asthma	0.1051/0.6120	0.0464/0.7035	0.0429/0.7393	<b>0.0413/0.7672</b>
COPD	0.1089/0.5886	0.0544/0.7213	0.0436/0.7419	<b>0.0411/0.7601</b>
BE	0.1348/0.5675	0.0494/0.7184	0.0448/0.7366	<b>0.0392/0.7830</b>
CI	0.0953/0.6033	0.0487/0.7300	0.0473/0.7219	<b>0.0446/0.7514</b>
PT	0.0857/0.6071	0.0469/0.7232	0.0424/0.7427	<b>0.0386/0.7692</b>
PN	0.1297/0.5679	0.0556/0.6878	0.0513/0.7077	<b>0.0491/0.7298</b>
Total	0.1142/0.5896	0.0530/0.7108	0.0460/0.7307	<b>0.0435/0.7558</b>

<sup>a</sup>The lowest MAE and highest SSIM values are bold faced.

through the zero-filling, CS-MRI, and CasNet are shown in Figure 4B2,C2,D2, respectively. It can be seen that there are serious noises in Figure 4A2, and severe undersampling artifacts exist in Figure 4B2. The artifacts linger in the CS-MRI results. However, after the CasNet, the artifacts are successfully removed and most of the lung details are restored, especially in the green boxes in Figure 4D2. The CasNet can improve the conspicuity of detailed tissues and sharp boundaries of the lung, which is not accessible with

the CS-MRI. Moreover, the CasNet holds the lowest MAE and highest SSIM values.

The quantitative measures for all test data through the CS-MRI are also listed in Table 2. It can be seen that the CasNet outperforms the CS-MRI in terms of MAE with a decrease by 21.42%, 10.99%, 24.45%, 20.65%, 8.42%, 17.70%, and 11.69% for the healthy, asthma, COPD, BE, CI, PT, and PN sets, and SSIM with an increase by 6.80%, 9.05%, 5.38%, 8.99%, 2.93%, 6.36%, and 6.11%, respectively. For

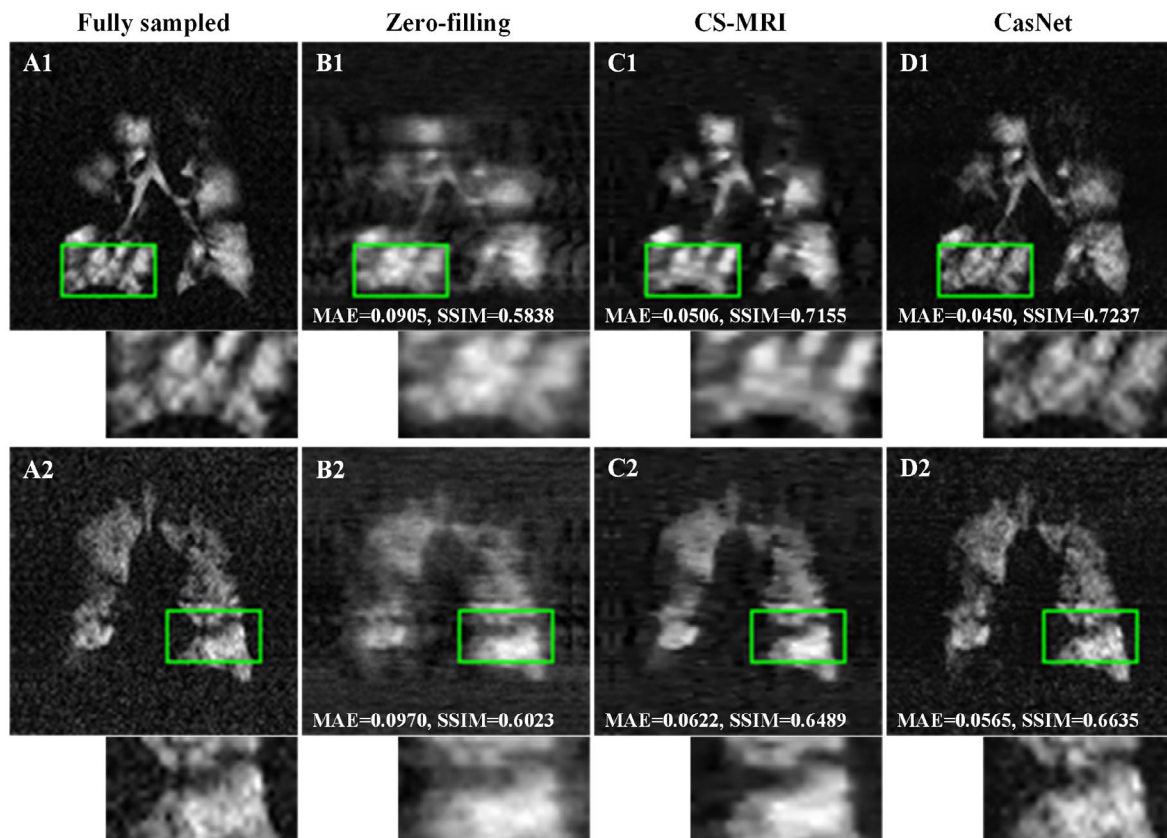


**FIGURE 4** Reconstructed results obtained using the zero-filling, CS-MRI, and CasNet at an AF of 4. A1, One slice of FS image from a COPD volunteer. A2, One slice of FS image from a PN subject. B1-B2,C1-C2,D1-D2, Reconstructed results obtained using the zero-filling, CS-MRI and CasNet, respectively. Magnified regions of green boxes are placed at the right bottom of the corresponding images. The quantitative metrics are also listed under the images

the total test data, the MAE decreases by 17.92% and SSIM increases by 6.33%. Furthermore, the reconstruction time is significantly reduced through the CasNet. Once the training is completed, the reconstruction is extremely efficient without adjusting additional parameters. The overall reconstruction time for the 87 images is 2.7 s (approximately 31 ms for 1 slice). In comparison, it is time-consuming to optimize the hyper-parameters in the CS-MRI. Even if the parameters have been selected, the reconstruction time for the CS-MRI with 64 iterations is approximately 2600 ms for 1 slice on CPU.

### 3.3 | VDP

For all test data, Figure 5A shows the scatter plot of VDP values calculated from the FS and reconstructed images through the CasNet. A good correlation can be observed ( $r = 0.975$ ;  $P < 0.001$ ). Figure 5B shows the Bland-Altman plot of the 2 measurements, where the mean bias  $\pm$  standard deviation is  $0.01\% \pm 0.91\%$  (95% limit of agreement:  $-1.77\%$  to  $1.79\%$ ). This indicates that the VDP values of the FS and reconstructed images are in close agreement.

Figure 5C shows the VDP comparisons between the FS and reconstructed images for the total, healthy, COPD, BE, CI, PT, and PN test data. Because the asthma set only contains 2 images, the comparison for this category is excluded. We can see that there are no significant differences regarding VDP between the FS and reconstructed images for all the clinical indications ( $P > 0.05$ ).

### 3.4 | In vivo

Figure 6A1,A2 shows the FS images from 2 healthy subjects, and the prospectively undersampled results by means of the zero-filling and CasNet are shown in Figure 6B1-B2 and C1-C2, respectively. Figure 6D1,D2,E1,E2 show the cluster

maps of A1,A2,C1,C2, respectively. Serious artifacts are observed in the zero-filling images. Accordingly, it is difficult to represent structural details of the lung. However, through the CasNet, such artifacts are successfully removed, and some detailed structures appear sharp (see Figure 6C1,C2). This is helpful to delineate fine details of the lung. Figure 6A3-A4 display the FS images from 2 asymptomatic smokers, which exist obvious ventilation defect regions. Similar ventilation defects can also be identified in Figure 6C3,C4. However, such regions are covered by undersampling artifacts in Figure 6B3,B4.

The VDP, SNR, and SSIM terms are listed under each image in Figure 6. The VDP values derived from Figure 6C1-C4 remain consistent with those from Figure 6A1-A4, confirming good preservation of the ventilation distribution with the CasNet. Moreover, the highest SNR values are obtained by using the CasNet. Because the FS and undersampled data are acquired in 2 different breath-holds, the same slices from these 2 datasets are inherently misregistered and clearly not identical.<sup>12,39</sup> Accordingly, direct quantitative comparisons between the prospective and FS images exhibit worse SSIM values than those of the retrospective results.

A summary of metrics for the 10 subjects is provided in Table 3. It can be found a good VDP agreement between the FS and reconstructed images for both the healthy subjects and asymptomatic smokers (no significant differences). Compared with the FS images, SNR values of the reconstructed images are significantly higher ( $P < 0.001$ ).

## 4 | DISCUSSION

### 4.1 | Cascaded CNNs

Recently, deep learning is fascinated in the field of MRI reconstruction.<sup>23-26</sup> To our best knowledge, no study has

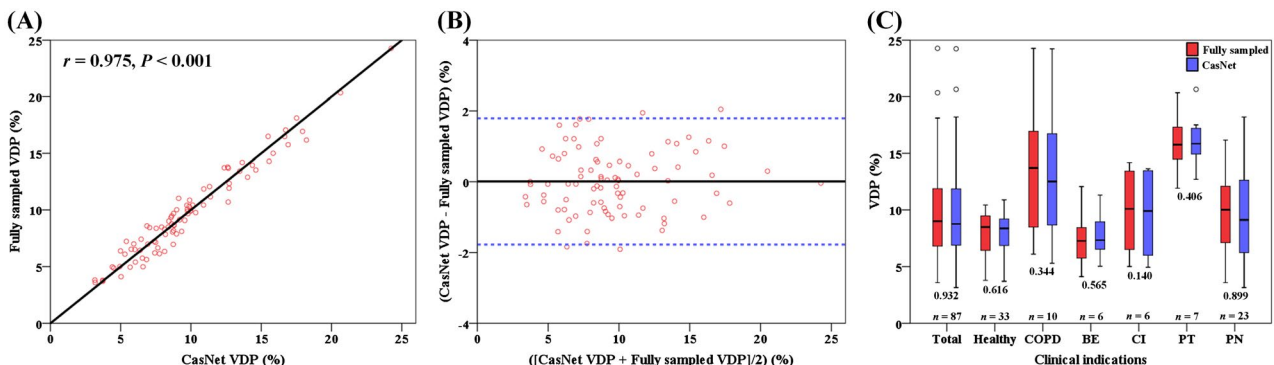


**FIGURE 5** VDP comparisons between the FS and reconstructed images through the CasNet at an AF of 4. A, Scatter plot of VDP for all test data. Solid line indicates the line of equality. B, Bland-Altman plot shows the mean bias ( $\pm$  standard deviation) in terms of VDP is  $0.01\% \pm 0.91\%$  (lower limit =  $-1.91\%$  and upper limit =  $2.05\%$ ) between the FS and reconstructed images for all test data. Solid line indicates the mean difference and dotted lines indicate the 95% limits of agreement. C, Boxplot of VDP of the FS and reconstructed images for different clinical indications.  $P$  values are listed under each category,  $n$  is the image number of each category



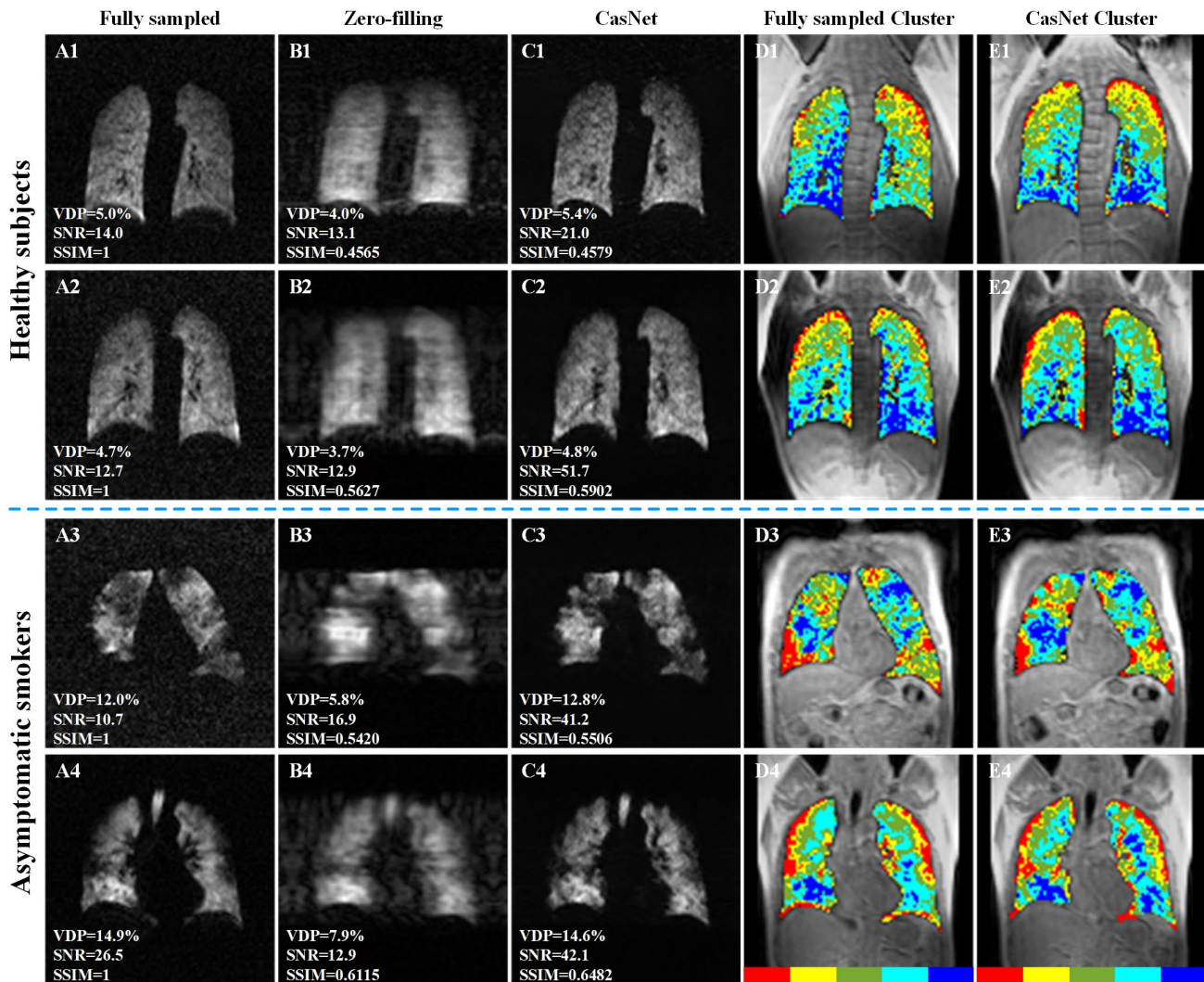


**FIGURE 6** Reconstructed results of the prospective acquisition from healthy subjects and asymptomatic smokers at an AF of 4. A1-A2, 2 slices of FS images from 2 healthy subjects. A3-A4, 2 slices of FS images from 2 asymptomatic smokers. B1-B4, C1-C4, Reconstructed results obtained using the zero-filling and CasNet, respectively. VDP, SNR, and SSIM values are listed under the images. D1-D4, Cluster maps of ventilation regions of (A1-A4). E1-E4, Cluster maps of ventilation regions of (C1-C4). Clusters represent the gradations of signal intensity, and red color denotes ventilation defect regions

investigated the applicability of deep learning to HP gas MRI reconstruction. In this study, we develop a CasNet model for HP gas MRI reconstruction from highly undersampled k-space data, aiming to accelerate the imaging speed or acquire more data. In the CasNet, the C-net can remove undersampling artifacts and restore partial details of the lung, and the F-net can further refine structural details of the lung by leveraging  $^1\text{H}$  image prior knowledge.

Experimental results validate that the CasNet can effectively reconstruct HP gas ventilation images at an AF of 4. As shown in Figures 3 and 4, undersampling artifacts are successfully removed and detailed structures of the lung are well restored. For all test data, the MAE is 4.35% and the SSIM is 0.7558. However, the MAE becomes 5.30% and SSIM turns into 0.7108 through the CS-MRI. This indicates

that the CasNet is superior to the baseline methods (such as, zero-filling and CS-MRI). For different clinical indications, a good VDP agreement is observed between the FS and reconstructed images through the CasNet. Furthermore, the CasNet is validated on prospective acquisitions for 5 healthy subjects and 5 asymptomatic smokers, which effectively preserves edge sharpness and fine structures of the lung. There are no significant differences regarding VDP term between the FS and prospectively undersampled datasets. Although the training of CasNet may be time-consuming, it can rapidly reconstruct HP gas images once the training procedure is completed (approximately 31 ms for reconstructing 1 image). This indicates that the CasNet satisfies the needs of real-time reconstruction, while holding good reconstruction performance at high AFs.

**TABLE 3** Comparisons of VDP and SNR between the FS and reconstructed images through the CasNet for the healthy subjects and asymptomatic smokers

Subjects	FEV <sub>1</sub> /FVC (%)	VDP (%)		SNR	
		FS	CasNet	FS	CasNet
Healthy subjects					
HS1	84.5	4.1 ± 1.1	4.7 ± 1.3	14.9 ± 1.6	24.5 ± 3.5
HS2	94.9	6.7 ± 1.3	7.2 ± 2.0	15.4 ± 2.2	49.4 ± 4.4
HS3	87.9	5.1 ± 1.6	5.6 ± 1.8	15.7 ± 1.6	52.7 ± 7.5
HS4	82.1	6.7 ± 1.1	6.3 ± 1.2	15.6 ± 1.9	47.2 ± 4.3
HS5	88.3	4.7 ± 1.0	5.0 ± 1.4	28.0 ± 2.0	50.7 ± 5.5
Mean	87.5 ± 4.8	5.5 ± 1.6	5.8 ± 1.8	18.0 ± 5.5	44.6 ± 11.8
<i>P</i> -value		0.102		<0.001	
Asymptomatic smokers					
AS1	68.7	26.7 ± 13.9	27.8 ± 15.0	13.8 ± 1.6	34.9 ± 9.6
AS2	82.4	5.9 ± 1.4	5.4 ± 2.0	24.7 ± 2.1	50.8 ± 6.8
AS3	89.2	7.2 ± 2.1	7.6 ± 2.5	13.2 ± 3.1	43.4 ± 4.9
AS4	77.9	9.2 ± 1.8	9.5 ± 2.2	27.3 ± 3.9	49.7 ± 5.1
AS5	70.3	8.9 ± 3.3	9.7 ± 2.6	26.7 ± 3.1	46.2 ± 4.8
Mean	77.7 ± 8.5	11.6 ± 10.0	12.0 ± 10.6	21.3 ± 6.6	44.9 ± 8.6
<i>P</i> -value		0.125		<0.001	

## 4.2 | Performance comparisons

Owing to the effective de-aliasing performance of U-Net, the C-net can remove aliasing artifacts, even at high AFs. This is consistent with other results in previous works.<sup>29,30,45</sup> However, some structural details are still blurred and distorted in the lung, as shown in Figure 3C1,C2. The reason may be that the training data is corrupted by noise, which prevents the CNNs from learning the mapping between the zero-filling and reference images.<sup>16,25,26</sup> Nevertheless, high-quality (even noiseless) training data are difficult or impossible to acquire due to the nonrenewability of HP magnetization. Thus, a refine stage is adopted to restore those blurred details by incorporating prior knowledge provided by <sup>1</sup>H images (the reconstruction loss is only within the lung region and the background noise is excluded). In this case, the F-net focuses on the reconstruction within the lung, which improves its robustness and repeatability. Both qualitative and quantitative results indicate that the refinement procedure can effectively improve structural details and sharpness of the lung. In fact, the L2 loss incorporating prior knowledge has been successfully applied in diverse fields. For example, the weighted context loss in semantic image inpainting also used the prior knowledge of binary mask to pay more attention to missing regions rather than background ones.<sup>46,47</sup>

From Figure 4C1,C2, it can be found that the CS-MRI is inferior for removing artifacts and restoring fine details at high AFs. It is known that CS-MRI with global sparsifying transforms is normally limited to the AF of 2.5 to 3.<sup>48</sup> When the AF is set to 4, there exist distinct undersampling artifacts

in the CS-MRI results.<sup>25,30</sup> In contrast, the CasNet performs consistently well in various clinical indications (see Figures 3 and 4, and Table 2). In particular, the substantial ventilation defects in Figure 4A1 are correctly depicted in Figure 4D1. This is useful for examining structural and functional abnormalities in COPD.<sup>43</sup>

It should be noted that the fine details are largely regularized in Figure 3, which is most likely due to the use of training data with various clinical indications. Minimizing the L2 loss between the FS and reconstructed results drives the CNNs to search pixel-wise averages of plausible solutions, which are typically overly smooth and have poor perceptual quality.<sup>49</sup> In the future, it will be interesting to evaluate the performance of CasNet when training with the subset of ventilation images from different clinical indications, e.g., asthma, COPD.

## 4.3 | In vivo

As for the prospective datasets, the CasNet provides a good agreement with FS images. A negligible bias in VDP values is obtained for both the healthy subjects and asymptomatic smokers, suggesting the clinical potential of the CasNet in real accelerated acquisition.

The reconstructed images through the CasNet have higher SNR values than FS images in Figure 6 and Table 3. This can be attributed to higher FA in the prospectively undersampled acquisition. The large FA results in high signal intensity in the k-space center, which determines the overall SNR of MR images.<sup>12</sup> This is consistent with the results previously

reported in Ajraoui et al.<sup>11</sup> Moreover, CNN-based reconstruction methods can function as a de-noising network for images with low SNR, which may also result in the increase of SNR in the reconstructed images.<sup>50</sup>

#### 4.4 | AF

For higher AFs (e.g., 6 or 8), we investigate the feasibility of the CasNet. Figure 7A displays the FS image of the 17<sup>th</sup> slice of the lung from a healthy volunteer. Under different AFs, the retrospectively undersampled results through the zero-filling and CasNet are displayed in Figure 7B1-B3, C1-C3, respectively. It can be found that the zero-filling images not only become more blurred but also lose more fine details with increasing AFs (The MAE values ascend and the SSIM values descend). However, after the CasNet, the artifacts are well eliminated and the sharp structures are well restored, especially in the green boxes in Figure 7C1-C3. Although Figure 7C3 has inferior quantitative metrics, the lung structure is well preserved. This means that the CasNet has potential for reconstructing HP gas MRI at high AFs.

It should be noted that the AF used in the latest brain MRI reconstruction is even up to 10.<sup>17</sup> Nevertheless, the image size is  $256 \times 256$ , and the number of training data is 16,095 in that

work (approximately 21 times larger than that used in this work). Therefore, the brain MRI reconstruction is effective because there are large number of available samples during the training stage. Accordingly, we will further collect massive data to train the reliability of the CasNet, and then achieve higher AFs.

#### 4.5 | Limitations

Although the CasNet generates promising results for HP gas MRI reconstruction, there are some limitations to this study. First, the number of good-quality references is insufficient because it is difficult to acquire HP gas images with high spatial resolution and SNR. However, large amounts of training data are required to train reliable and efficacious deep learning models. Therefore, the further work is to collect massive data with high quality. Second, zero-filling results are deemed as the input of the CasNet, whose quality is deteriorated by undersampling artifacts. If the AF becomes larger, the deterioration tends to become more serious.<sup>11</sup> In this way, the CasNet possibly loses fine details of the lung. This leads to a linchpin for our further work, for example, further exploiting the 3D spatial correlations from adjacent slices in volumetric images, using undersampled k-space as input

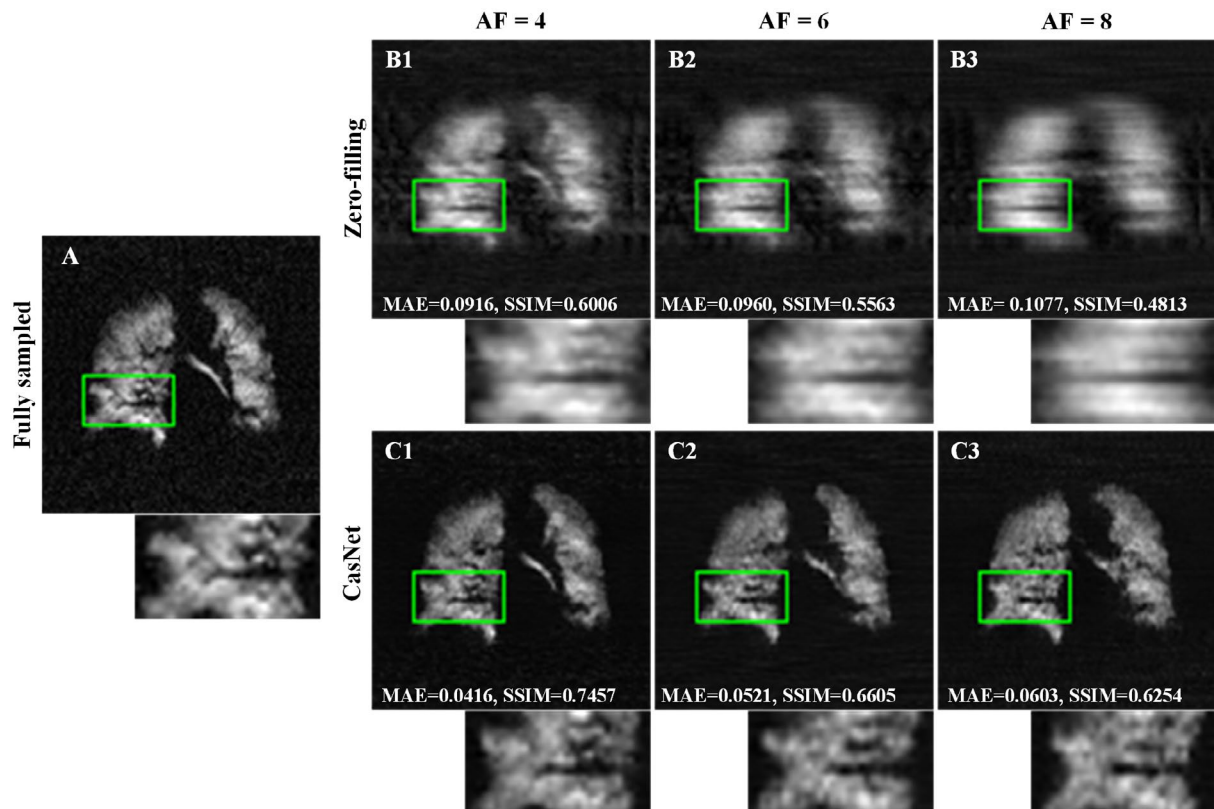


**FIGURE 7** Under different AFs, the reconstructed results are obtained using the zero-filling and CasNet. A, 1 slice of FS images from a healthy volunteer. When the AFs are set to 4, 6, and 8, the corresponding reconstructed results through the zero-filling and CasNet are displayed in (B1-B3) and (C1-C3), respectively. Magnified regions of green boxes are placed at the right bottom of the corresponding images. The MAE and SSIM values are also listed on the images

and optimizing undersampling patterns in the training, combining with the perceptual loss and generative adversarial networks.<sup>49</sup> Third, although U-Net is applied in the CasNet, other advanced network architectures such as dense convolutional network<sup>51</sup> will be compatible in the future. Fourth, L2 loss functions are used in the CasNet, which may not be optimal for undersampled HP gas MRI reconstruction. Additional loss functions, such as the L1 norm, SSIM, will be further explored. Fifth, the CasNet only focuses on variable-density Cartesian acquisition. In the future, a similar CNNs model with appropriate modifications will be extended to non-Cartesian acquisition, including radial and spiral trajectories. Lastly, the validity of the CasNet on prospective acquisition is tested on 5 healthy volunteers and 5 asymptomatic smokers. Massive in vivo experiments should be done to demonstrate the robustness and effectiveness of the CasNet.

## 5 | CONCLUSIONS

In this work, we present a CasNet for fast and accurately reconstructing human lung gas MRI from highly undersampled k-space. The CasNet consists of a coarse net for de-aliasing, and a fine net for restoring structural details within lung regions. Experimental results demonstrate that the CasNet is able to not only improve reconstruction performance but also have some advantages in comparisons with the baseline methods. Once the training of CasNet is completed, the reconstruction process is extremely fast (tens of ms per 2D slice), which enables possible real-time reconstruction of human lung. Moreover, VDP values provided by the reconstructed results agree well with those of the reference standard. As for the prospective datasets, there are no significant differences between the FS and reconstructed images regarding VDP term, but the CasNet has significantly higher SNR values. Consequently, the CasNet is promising in real-time imaging of human lung and facilitating the study of clinical lung diseases.

## ACKNOWLEDGMENTS

The authors would like to gratefully acknowledge the support from NVIDIA Corporation for providing us the TITAN Xp GPU used in this work. Caohui Duan, He Deng, and Xin Lou contributed equally to this work.

## ORCID

Xin Zhou  <https://orcid.org/0000-0002-5580-7907>

## REFERENCES

- Mugler JP III, Altes TA. Hyperpolarized <sup>129</sup>Xe MRI of the human lung. *J Magn Reson Imaging*. 2013;37:313–331.
- Zhou X, Graziani D, Pines A. Hyperpolarized xenon NMR and MRI signal amplification by gas extraction. *Proc Natl Acad Sci U S A*. 2009;106:16903–16906.
- Deng H, Zhong J, Ruan W, et al. Constant-variable flip angles for hyperpolarized media MRI. *J Magn Reson*. 2016;263:92–100.
- Lee RF, Johnson G, Grossman RI, Stoeckel B, Trampel R, McGuinness G. Advantages of parallel imaging in conjunction with hyperpolarized helium—a new approach to MRI of the lung. *Magn Reson Med*. 2006;55:1132–1141.
- Wild JM, Paley MNJ, Kasuboski L, et al. Dynamic radial projection MRI of inhaled hyperpolarized <sup>3</sup>He gas. *Magn Reson Med*. 2003;49:991–997.
- Salerno M, Altes TA, Brookeman JR, de Lange EE, Mugler JP III. Dynamic spiral MRI of pulmonary gas flow using hyperpolarized <sup>3</sup>He: preliminary studies in healthy and diseased lungs. *Magn Reson Med*. 2001;46:667–677.
- Xiao S, Deng H, Duan C, et al. Considering low-rank, sparse and gas-inflow effects constraints for accelerated pulmonary dynamic hyperpolarized <sup>129</sup>Xe MRI. *J Magn Reson*. 2018;290:29–37.
- Ruppert K, Amzajerdian F, Hamedani H, et al. Rapid assessment of pulmonary gas transport with hyperpolarized <sup>129</sup>Xe MRI using a 3D radial double golden-means acquisition with variable flip angles. *Magn Reson Med*. 2018;80:2439–2448.
- Kern AL, Gutberlet M, Voskrebenezov A, et al. Mapping of regional lung microstructural parameters using hyperpolarized <sup>129</sup>Xe dissolved-phase MRI in healthy volunteers and patients with chronic obstructive pulmonary disease. *Magn Reson Med*. 2019;81:2360–2373.
- Lustig M, Donoho D, Pauly JM. Sparse MRI: the application of compressed sensing for rapid MR imaging. *Magn Reson Med*. 2007;58:1182–1195.
- Ajraoui S, Lee KJ, Deppe MH, Parnell SR, Parra-Robles J, Wild JM. Compressed sensing in hyperpolarized <sup>3</sup>He Lung MRI. *Magn Reson Med*. 2010;63:1059–1069.
- Ajraoui S, Parra-Robles J, Wild JM. Incorporation of prior knowledge in compressed sensing for faster acquisition of hyperpolarized gas images. *Magn Reson Med*. 2013;69:360–369.
- Chan HF, Stewart NJ, Parra-Robles J, Collier GJ, Wild JM. Whole lung morphometry with 3D multiple b-value hyperpolarized gas MRI and compressed sensing. *Magn Reson Med*. 2017;77:1916–1925.
- Zhang H, Xie J, Xiao S, et al. Lung morphometry using hyperpolarized <sup>129</sup>Xe multi-b diffusion MRI with compressed sensing in healthy subjects and patients with COPD. *Med Phys*. 2018;45:3097–3108.
- Block KT, Uecker M, Frahm J. Undersampled radial MRI with multiple coils: iterative image reconstruction using a total variation constraint. *Magn Reson Med*. 2007;57:1086–1098.
- Hammernik K, Klatzer T, Kobler E, et al. Learning a variational network for reconstruction of accelerated MRI data. *Magn Reson Med*. 2018;79:3055–3071.
- Yang G, Yu S, Dong H, et al. Dagan: deep de-aliasing generative adversarial networks for fast compressed sensing MRI reconstruction. *IEEE Trans Med Imaging*. 2018;37:1310–1321.
- LeCun Y, Bengio Y, Hinton G. Deep learning. *Nature*. 2015;521:436–444.
- Krizhevsky A, Sutskever I, Hinton GE. Imagenet classification with deep convolutional neural networks. In: Advances in Neural Information Processing Systems (NIPS), Lake Tahoe, NV, 2012. pp. 1097–1105.
- Kim J, Lee JK, Lee KM. Accurate image super-resolution using very deep convolutional networks. In Proceedings of the IEEE

- Conference on Computer Vision and Pattern Recognition (CVPR), Seattle, WA, 2016. pp. 1646–1654.
21. Zhang K, Zuo W, Chen Y, Meng D, Zhang L. Beyond a Gaussian denoiser: residual learning of deep CNN for image denoising. *IEEE Trans Image Process.* 2017;26:3142–3155.
  22. Ronneberger O, Fischer P, Brox T. U-net: convolutional networks for biomedical image segmentation. In: International Conference on Medical Image Computing and Computer-Assisted Intervention (MICCAI), Munich, Germany, 2015. pp. 234–241.
  23. Schlemper J, Caballero J, Hajnal JV, Price AN, Rueckert D. A deep cascade of convolutional neural networks for dynamic MR image reconstruction. *IEEE Trans Med Imaging.* 2018;37:491–503.
  24. Wang S, Su Z, Ying L, et al. Accelerating magnetic resonance imaging via deep learning. In: Proceedings of the IEEE 13th International Symposium on Biomedical Imaging (ISBI), Prague, Czech Republic, 2016. pp. 514–517.
  25. Eo T, Jun Y, Kim T, Jang J, Lee H-J, Hwang D. KIKI-net: cross-domain convolutional neural networks for reconstructing undersampled magnetic resonance images. *Magn Reson Med.* 2018;80:2188–2201.
  26. Knoll F, Hammernik K, Kobler E, Pock T, Recht MP, Sodickson DK. Assessment of the generalization of learned image reconstruction and the potential for transfer learning. *Magn Reson Med.* 2018;81:116–128.
  27. Oktay O, Ferrante E, Kamnitsas K, et al. Anatomically constrained neural networks (ACNNs): application to cardiac image enhancement and segmentation. *IEEE Trans Med Imaging.* 2018;37:384–395.
  28. Tahir BA, Holsbeke CV, Ireland RH, et al. Comparison of CT-based lobar ventilation with <sup>3</sup>He MR imaging ventilation measurements. *Radiology.* 2015;278:585–592.
  29. Jin KH, McCann MT, Froustey E, Unser M. Deep convolutional neural network for inverse problems in imaging. *IEEE Trans Image Process.* 2017;26:4509–4522.
  30. Han Y, Yoo J, Kim HH, Shin HJ, Sung K, Ye JC. Deep learning with domain adaptation for accelerated projection-reconstruction MR. *Magn Reson Med.* 2018;80:1189–1205.
  31. Ioffe S, Szegedy C. Batch normalization: accelerating deep network training by reducing internal covariate shift. arXiv preprint, 2015. arXiv:1502.03167.
  32. Stewart NJ, Norquay G, Griffiths PD, Wild JM. Feasibility of human lung ventilation imaging using highly polarized naturally abundant xenon and optimized three-dimensional steady-state free precession. *Magn Reson Med.* 2015;74:346–352.
  33. He M, Zha W, Tan F, Rankine L, Fain S, Driehuys B. A comparison of two hyperpolarized <sup>129</sup>Xe MRI ventilation quantification pipelines: the effect of signal to noise ratio. *Acad Radiol.* 2019;26:949–959.
  34. Wild JM, Paley MN, Viallon M, Schreiber WG, van Beek EJ, Griffiths PD. *k*-Space filtering in 2D gradient-echo breath-hold hyperpolarized <sup>3</sup>He MRI: spatial resolution and signal-to-noise ratio considerations. *Magn Reson Med.* 2002;47:687–695.
  35. Wild JM, Teh K, Woodhouse N, et al. Steady-state free precession with hyperpolarized <sup>3</sup>He: experiments and theory. *J Magn Reson.* 2006;183:13–24.
  36. Deppe MH, Wild JM. Variable flip angle schedules in bSSFP imaging of hyperpolarized noble gases. *Magn Reson Med.* 2012;67:1656–1664.
  37. Vedaldi A, Lenc K. Matconvnet: convolutional neural networks for matlab. In: Proceedings of the 23rd ACM International Conference on Multimedia, New York, NY, 2015. pp. 689–692.
  38. Glorot X, Bengio Y. Understanding the difficulty of training deep feedforward neural networks. In: Proceedings of the 13th International Conference on Artificial Intelligence and Statistics, Sardinia, Italy, 2010. pp. 249–256.
  39. Collier GJ, Hughes PJC, Horn FC, et al. Single breath-held acquisition of coregistered 3D <sup>129</sup>Xe lung ventilation and anatomical proton images of the human lung with compressed sensing. *Magn Reson Med.* 2019;82:342–347.
  40. Qing K, Altes TA, Tustison NJ, et al. Rapid acquisition of helium-3 and proton three-dimensional image sets of the human lung in a single breath-hold using compressed sensing. *Magn Reson Med.* 2015;74:1110–1115.
  41. Sweldens W. The lifting scheme: a construction of second generation wavelets. *Siam J Math Anal.* 1998;29:511–546.
  42. Wang Z, Bovik AC, Sheikh HR, Simoncelli EP. Image quality assessment: from error visibility to structural similarity. *IEEE Trans Image Process.* 2004;13:600–612.
  43. Driehuys B, Martinez-Jimenez S, Cleveland ZI, et al. Chronic obstructive pulmonary disease: safety and tolerability of hyperpolarized <sup>129</sup>Xe MR imaging in healthy volunteers and patients. *Radiology.* 2012;262:279–289.
  44. Kirby M, Heydarian M, Svenningsen S, et al. Hyperpolarized <sup>3</sup>He magnetic resonance functional imaging semiautomated segmentation. *Acad Radiol.* 2012;19:141–152.
  45. Hauptmann A, Arridge S, Lucka F, Muthurangu V, Steeden JA. Real-time cardiovascular MR with spatio-temporal artifact suppression using deep learning-proof of concept in congenital heart disease. *Magn Reson Med.* 2019;81:1143–1156.
  46. Yeh RA, Chen C, Lim TY, Schwing AG, Hasegawa-Johnson M, Do MN. Semantic image inpainting with deep generative models. In: Proceedings of the IEEE Conference on Computer Vision and Pattern Recognition (CVPR), Honolulu, HI, 2017. p. 4.
  47. Song C, Huang Y, Ouyang W, Wang L. Mask-guided contrastive attention model for person re-identification. In: Proceedings of the IEEE Conference on Computer Vision and Pattern Recognition (CVPR), Salt Lake City, UT, 2018. pp. 1179–1188.
  48. Ravishanker S, Bresler Y. MR image reconstruction from highly undersampled *k*-space data by dictionary learning. *IEEE Trans Med Imaging.* 2011;30:1028–1041.
  49. Ledig C, Theis L, Huszár F, Caballero J, Cunningham A. Photo-realistic single image super-resolution using a generative adversarial network. In: Proceedings of the IEEE Conference on Computer Vision and Pattern Recognition (CVPR), Honolulu, HI, 2017. p. 4.
  50. Chen F, Taviani V, Malkiel I, et al. Variable-density single-shot fast spin-echo MRI with deep learning reconstruction by using variational networks. *Radiology.* 2018;289:366–373.
  51. Huang G, Liu Z, Van DM, Weinberger KQ. Densely connected convolutional networks. In: Proceedings of the IEEE Conference on Computer Vision and Pattern Recognition (CVPR), Honolulu, HI, 2017. p. 3.

**How to cite this article:** Duan C, Deng H, Xiao S, et al. Fast and accurate reconstruction of human lung gas MRI with deep learning. *Magn Reson Med.* 2019;82:2273–2285. <https://doi.org/10.1002/mrm.27889>